Experiments and Numerical Implementation of a Boundary Value Problem Involving a Magnetorheological Elastomer Layer Subjected to a Nonuniform Magnetic Field

Charles Dorn
Graduate Aerospace Laboratories,
California Institute of Technology,
Pasadena, CA 91125
e-mail: cdorn@caltech.edu

Laurence Bodelot[1]
Solid Mechanics Laboratory (LMS),
CNRS, Ecole Polytechnique,
Institut Polytechnique de Paris,
91128 Palaiseau, France
e-mail: laurence.bodelot@polytechnique.edu

Kostas Danas
Solid Mechanics Laboratory (LMS),
CNRS, Ecole Polytechnique,
Institut Polytechnique de Paris,
91128 Palaiseau, France
e-mail: konstantinos.danas@polytechnique.edu

This study investigates experimentally and numerically the response of a magnetorheological elastomer (MRE) layer placed atop an electromagnetic coil. The MRE layer is deflected upon application of a current in the coil, which creates highly nonuniform magnetic fields. Isotropic and transversely isotropic layers (i.e., containing chains of magnetic particles) are tested experimentally, and the isotropic layer exhibits the largest deflection. To enhance the energetic efficiency of the model device, an iron core is introduced inside the electromagnetic coil, thereby leading to an increase in the resulting magnetic field near the center of the MRE layer. In parallel, the boundary value problem —including the MRE layer, the coil, the core (if present) and the surrounding air—is modeled numerically. For this, a magneto-mechanical, vector potential-based variational formulation is implemented in a standard three-dimensional finite element model at finite strains. For the material description, a recently proposed analytical homogenization-guided model is used to analyze the MRE in the "coil-only" configuration. It is then employed to predict the response of the layer in the "coil plus core" configuration, thus circumventing the need for a separate material characterization procedure. The proposed numerical simulation strategy provides a deeper understanding of the underlying complexity of the magnetic fields and of their interaction with the MRE layer. This study also reveals the importance of modeling the entire setup for predicting the response of MRE materials and, as a result, constitutes a step toward designing more efficient MRE-based devices. [DOI: 10.1115/1.4050534]

Keywords: computational mechanics, mechanical properties of materials, micromechanics, structures

1 Introduction

Magnetorheological elastomers (MREs) are man-made smart composite materials obtained by dispersing magnetic particles in an elastomer matrix. Rigbi and Jilken [1] have been the first to conduct tests on MREs and thereby to introduce previously unknown magneto-mechanical effects in soft polymers. Indeed, the soft mechanical behavior of the matrix, combined with the magnetic properties of the particles, allows these flexible composites not only to alter their viscoelastic properties and stiffness but also to exhibit large displacements and/or deformations in response to external magnetic fields. While the former effect can be exploited in controllable-stiffness devices for numerous advanced damping applications [2] (ranging from automobile [3–5] to prostheses [6] to adaptive materials applications [7,8]), the latter effect is of interest for haptic devices, shape control, actuators [9–11] or, more recently, for soft robotics [12–14].

MRE materials are thus undeniably appealing for modern high-tech applications. However, as pointed out in a recent review [11], they have been seldom utilized in commercial applications because the design of MRE-based devices has been so far devised only through a rather empirical approach. Previous studies presenting theoretical and numerical modeling of MRE [15–28] or h-MRE (i.e., with "hard" magnetic particles exhibiting large remanent magnetization) [22,23,29,30] samples or structures have largely focused on magneto-mechanical (microstructure-based or continuum-based) material modeling and on uniformly applied magnetic far fields. Moreover, despite a potential for slower time response applications in actuators or shape control, only a handful of studies have been dedicated to characterizing experimentally the coupled magneto-mechanical behavior of MREs (or of MRE-based structures and devices) under low-rate loadings [22,31–33]. Furthermore, in these experimental studies, the applied magnetic field has also been consistently uniform. For more information on this topic, the reader is referred to the recent review by Bastola and Hossain [34].

The present study builds upon works undertaken to characterize experimentally and theoretically the coupled magnetomechanical behavior of MREs at large strains and under large *uniform* magnetic fields. Specifically, a comprehensive experimental study [33] has revealed that characterization of the coupled magnetomechanical behavior of MRE materials necessitated specific samples and setups. In addition, shape effects and instabilities inherently present in MRE samples impose numerical parameter identification instead of straightforward analytical identification. Hence, in parallel, numerically assessed, microstructural analytical, explicit models have been developed for MREs allowing for an efficient numerical implementation in finite element codes [19,26,27]. Here, experiments and theory are combined to build and study a complete but highly nontrivial MRE-based boundary value problem (BVP) with nonuniform magnetic fields at finite strains, where material

[1]Corresponding author.

Manuscript received January 28, 2021; final manuscript received March 11, 2021; published online April 7, 2021. Assoc. Editor: Jizhou Song.

identification is performed directly within the proposed device. In particular, a simple model device (akin to a haptic surface) is proposed—consisting of a magnetorheological layer resting atop an electromagnetic coil—and tested for different MRE layer parameters (with or without particle field structuring) and configurations (presence or absence of an iron core in the electromagnetic coil). The MRE device is faithfully reproduced and numerically simulated with the finite element method. To model the device, a vector potential-based, finite-strain, magneto-mechanical variational formulation is proposed and implemented in three dimensions using standard finite elements with standard nodal connectivity. The simulations accurately capture the behavior of the device and produce reliable predictions of its behavior under a different configuration. Experiments serve as a benchmark for the numerical simulations, which in turn provide further insight into the magnetomechanical coupling mechanisms, as well as into the nonuniformity of the applied magnetic fields at play.

2 Experiments

2.1 Sample Fabrication. The MRE samples are made of a very soft and stretchable two-part silicone elastomer (Ecoflex 00-20 from Smooth-On Inc.) in which are dispersed soft (i.e., without remanence) iron particles having a 3.5 μm median diameter (carbonyl iron powder SM from BASF). For practical convenience during polymer fabrication, particle content is expressed in parts per hundred rubber (phr), which corresponds to the mass of particles per hundred parts of compounded elastomer mass. In this section, the corresponding volume fraction c of particles (see Ref. [33] for details on the conversion) is mentioned in parenthesis for clarity since such a quantity is relevant in the modeling of the magnetomechanical couplings and is used as such in Sec. 3. Samples of 70 phr ($c = 0.08$) are considered here. After mixing the particles without prior chemical treatment [33,35] in Part A of the silicone elastomer, Part B is added and the mix is further stirred thoroughly. The mix is then poured in a copper mold, shaped so as to yield an MRE disk 3 mm in thickness and 44 mm in diameter. The copper mold consists of heating plates so that curing of the samples (1 h at 70 °C) can either be performed outside or inside a magnetic field generated by a large electromagnet (more details on the fabrication procedure can be found in Ref. [33]). This leads, respectively, to either isotropic MRE samples or to transversely isotropic samples, also called "field-structured" samples, with particle chains aligned either within the plane of the disk (so-called perpendicular *to the subsequently applied magnetic field*) or along the thickness of the disk (so-called parallel *to the subsequently applied magnetic field*).

Overall, three types of 70 phr ($c = 0.08$) MRE disks are fabricated, denoted henceforth as isotropic, parallel, and perpendicular.

2.2 Setup. In the model device considered in this study, the magnetic field is generated by an electromagnetic coil manufactured by the Caylar company (France) and powered by a 20 V–20 A source. The winding is made with a pair of insulated copper wires 1.2 mm in diameter and contains 360 turns. The coil has the following dimensions: 20 mm inner diameter, 65 mm outer diameter, and 33 mm height. This coil is surrounded by a pure iron housing of 40 mm inner diameter and 90 mm outer diameter that offers extra space for 10 °C water provided by a chiller to circulate and cool down the system. A tapered pure iron core can be installed at the center of the coil to enhance the intensity of the magnetic field at the location where the MRE layer is to be installed. Note that the top of the iron core protrudes out of the coil. This coil within its iron housing is inserted in a 3D-printed plastic casing that permits placing and then clamping an MRE disk on top of the coil. The diameter of the MRE disk remaining outside of the clamp is then 30 mm, and the height of the clamping part of the casing is adjustable. A photograph of the electromagnetic coil and its tapered pure iron core is provided in Fig. 1(*a*), and a schematic of the complete

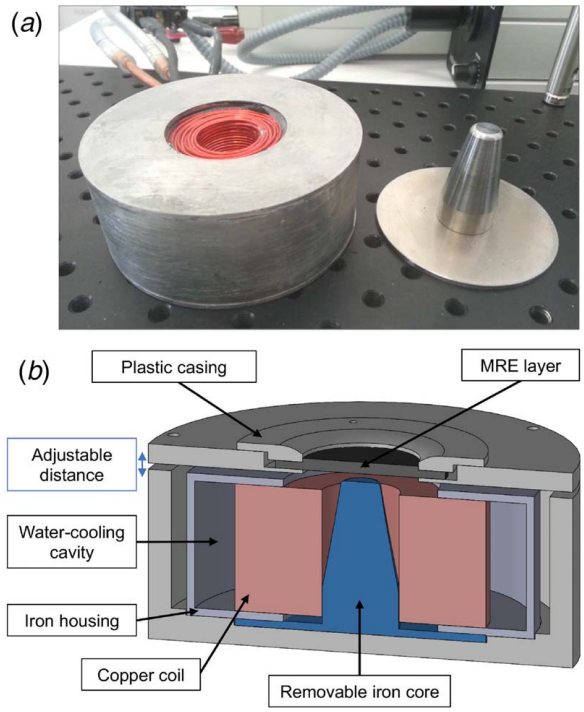

Fig. 1 (*a*) The coil surrounded by a pure iron housing (left) and the tapered iron core that can be placed at its center to enhance the generated magnetic field (right). (*b*) Schematic (cross section view along a symmetry plane) of the complete device comprising an MRE layer placed atop the electromagnetic coil with the iron core, iron housing, plastic casing, and clamp.

device, including the plastic casing and the clamp, is shown in Fig. 1(*b*).

Tests can be carried out either with or without the tapered iron core, and the MRE disk is then installed to maintain a vertical gap of 3 mm with either the top of the coil or the top of the iron core. When the iron core is not installed, the maximum current intensity applied to the electromagnetic coil is 20 A (restricted by the power source), whereas when the iron core is installed, the maximum applied intensity is chosen to be limited at 2.7 A. As a matter of fact, beyond this threshold, the layer is at risk of entering in contact with the core despite the spacer installed for elevating the disk and maintaining a 3 mm gap. This attests to the efficacy of the core in enhancing the magnetic field intensity at a given current and thus in reducing the need for current to power MRE-based devices.

During the experiments, the displacements at the surface of each MRE layer are monitored in situ by 3D digital image correlation (3D-DIC) using the CORRELATED SOLUTIONS software. This particular technique is selected because it permits an easy access to displacements at the surface of nonplanar objects. Unlike in previous works [36], the interest here is not in the full-field data provided by 3D-DIC but rather in the fact that it readily provides the deflection at the center of the layer without the errors that would be incurred by positioning and aligning a laser distance sensor. In accordance with the requirements of DIC [37], a random speckle pattern is applied onto the MRE layer using white spray paint (here, the sample itself constitutes a dark background). The MRE layer is lit symmetrically by two LED optical fibers to obtain proper contrast without reflections when the surface deforms. The deforming MRE layer is then imaged by two Pike 505-B cameras equipped with Tamron lenses and installed symmetrically on both sides of the prototype so as to form an angle with its normal (see Fig. 2). A calibration of the system with a normalized target permits the CORRELATED SOLUTIONS 3D-DIC software to locate the cameras in space and relate the displacements of the speckle pattern to the relative displacements of the layer in the three-dimensional space.

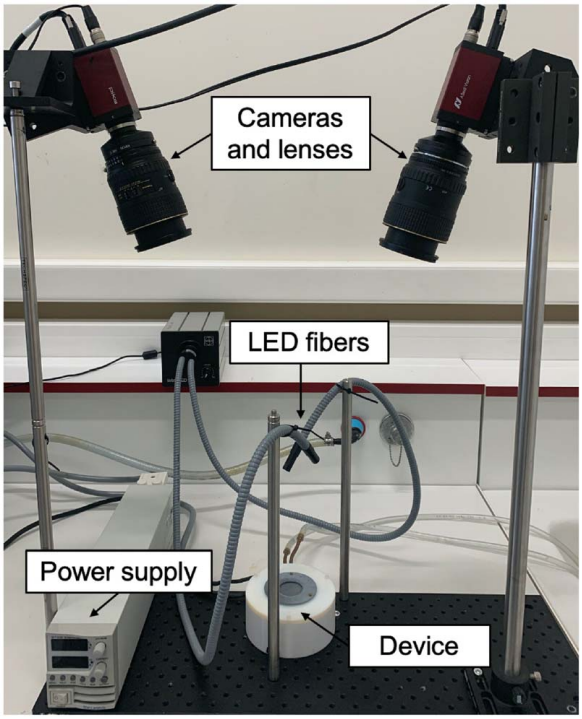

Fig. 2 3D-DIC experimental setup used to access the displacements at the surface of the MRE layers under the increasing magnetic field generated within the model device

2.3 Experimental Results. During each test, an increasing current intensity is applied to the electromagnetic coil, thus yielding an increasing magnetic field. Vertical displacement fields at the surface of the layer are obtained via 3D-DIC (see example in Fig. 3), and the vertical displacement at the center of the layer is extracted from these data for each value of the applied current. Three tests per configuration are conducted. Hence, in what follows, average values of the vertical displacement at the center of the upper surface of the layer are reported—along with error bars corresponding to a standard deviation—as a function of the applied current intensity for each test case (Figs. 4 and 5).

2.3.1 Effect of Particle Field Structuring. 70 phr ($c = 0.08$) MRE disk layers exhibiting particle field structuring as described in Sec. 2.1 (i.e., isotropic, perpendicular, and parallel *to the field*) are first tested in the device with no iron core. The vertical displacement at the center of their upper surfaces is plotted in Fig. 4 as the applied current increases.

Considering that the main direction of the magnetic field is along the revolution axis of the coil, the results plotted in Fig. 4 show that the smallest deflection is obtained when particle chains are parallel to the applied field. The maximum deflection appears in the case of the isotropic MRE layer, while the MRE layer with the particle chains aligned perpendicular to the magnetic field shows intermediate deflection.

These results shall be commented in light of those obtained in the context of the MRE material characterization conducted in Ref. [33] as well as of the instability results obtained in Ref. [32]. In the present device, the MRE sample is fairly slender, with its long dimension positioned perpendicular to the applied magnetic field.

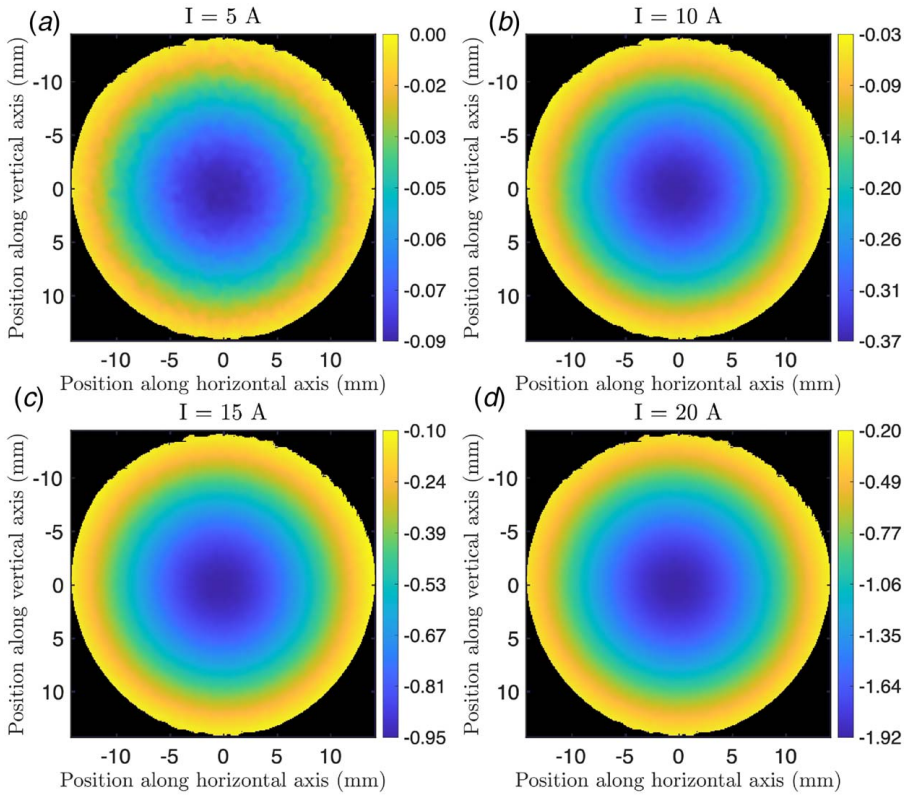

Fig. 3 Vertical displacement fields at the surface of the MRE layer (scale in millimeters) obtained via 3D-DIC in the case of the isotropic sample with no iron core, for different values of applied current: (*a*) 0.5 A, (*b*) 10 A, (c) 15 A, and (*d*) 20 A

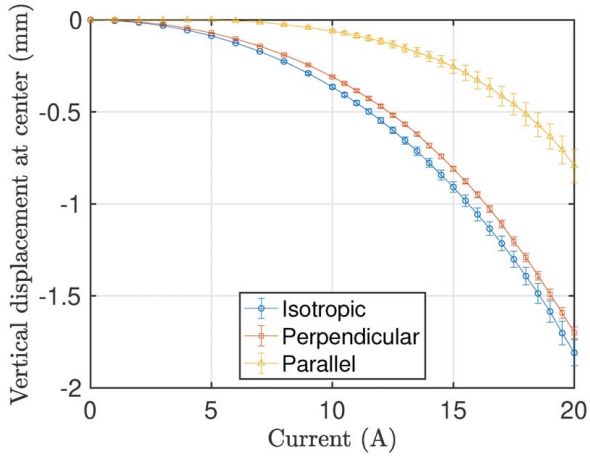

Fig. 4 Effect of particle field structuring on the device behavior: vertical displacement at the center of the upper surface of the disk for 70 phr (c = 0.08) disk layers that are isotropic, perpendicular, and parallel. The reported values correspond to the average over three tests conducted in the same configuration, and error bars represent a standard deviation.

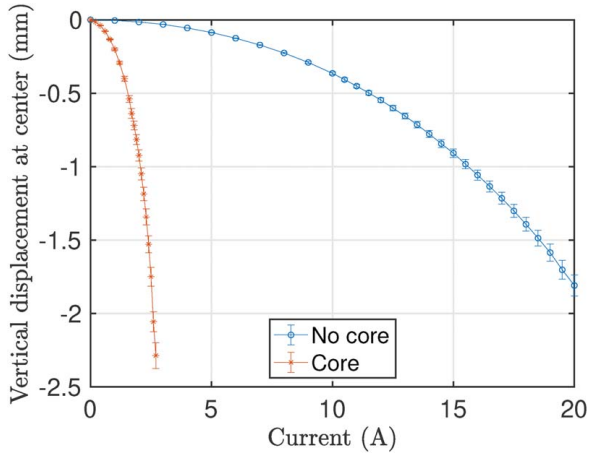

Fig. 5 Influence of the core on the device behavior: vertical displacement at the center of the upper surface of the disk for a 70 phr (c = 0.08) isotropic disk layer in the presence of and in the absence of the core. The reported values correspond to the average over three tests conducted in the same configuration, and error bars represent a standard deviation.

Hence, upon application of the magnetic field, a strong attraction of the MRE sample is observed, which is directly related to the well-known compass effect. This effect has been previously observed to cause overall sample instabilities (constrained by boundary conditions), which occur in all sample configurations—i.e., isotropic, parallel and perpendicular—as soon as the long dimension of the sample is perpendicular to the applied magnetic field [32,33]. In such a situation, large displacements/deflections are observed, and magnetostriction (i.e., field-induced deformation related to particle interactions) is no longer the predominant effect. Furthermore, it has been shown that particle chains have an effect akin to fibers in composite materials, thereby reinforcing the stiffness of the material along their direction. This effect is the largest when the particle chains are along the loading direction [33]. Consequently, under the deflection observed here, the parallel configuration is the stiffest mechanically among all configurations considered despite having the largest magnetic susceptibility along the particle chains [16,33,38]. This stiffness is further enhanced by the presence of the magnetic field, which, in this case, tends to keep the particles parallel to the field. The perpendicular configuration, even if known to be the most unstable [33,39], is also rather stiff mechanically due to the anisotropy induced by the particle chains. This interplay between the mechanical stiffness and magnetic properties leads to an optimal response obtained in the isotropic configuration. The latter is mechanically the softest of all, while any potential benefits of field structuring in the parallel and perpendicular configurations are, in the present case, outweighed by the corresponding mechanical stiffening.

2.3.2 Influence of the Core. In the following, focus is set on the optimal case of the isotropic MRE layer. It is further tested in the presence of the iron core, and the vertical displacement at the center of its upper surface is plotted in Fig. 5.

As expected, Fig. 5 readily shows that installing an iron core within the coil has a strong effect on the deflection evolution of the layer. Indeed, the iron core provokes a magnetic field concentration at the center of the MRE disk layer, as will be highlighted in the numerical simulations presented in Sec. 4.2. In the absence of an iron core, the maximum displacement attainable is −1.8 mm at 20 A, whereas, with the iron core installed, a displacement of −2.3 mm is obtained at the maximum applied current of 2.7 A. To highlight the influence of the core, one can remark that a displacement of −1.8 mm is reached at only about 2.5 A with the core versus 20 A with no core. This clearly demonstrates the interest of the iron core for lowering the input current. Note that no optimization was conducted for the design of the iron core, and this could be an interesting avenue to consider when power consumption is an important design parameter, or when power is supplied by standard batteries. This, nonetheless, requires the capacity to model such electromagnets and the nonuniform magnetic fields they generate, simultaneously with the resulting finite displacements and deformations of the soft components (e.g., the MRE layer in the present case).

3 Theory and Numerical Implementation

In this section, a general-purpose numerical framework capable of modeling the device is developed. To capture the full BVP, a vector potential-based magnetomechanical variational principle is proposed that can describe the MRE layer, electromagnetic coil, iron core, and surrounding air, *all with a single user-element definition*. Modeling all components of the device creates a useful and realistic problem setting where the sole input is the current applied to the coil, matching the experimental setting. Furthermore, detailed nonuniform magnetic fields can be captured since the air surrounding the device is modeled. Based on this framework, a three-dimensional finite element is implemented in finite strain.

3.1 A Single Variational Principle. First, a total Lagrangian variational formulation is established, from which a finite-strain, magneto-elastic, finite element framework is defined. More generally, consider a finite volume V with boundary ∂V occupied by a magneto-elastic material. A material point at position $\mathbf{X}$ in the undeformed configuration is mapped to $\mathbf{x}$ in the deformed configuration via the displacement vector $\mathbf{u}$ as $\mathbf{x} = \mathbf{X} + \mathbf{u}(\mathbf{X})$. The deformation gradient is then given by $\mathbf{F} = \mathbf{I} + \text{Grad}\,\mathbf{u}$, where Grad denotes the gradient operator with respect to $\mathbf{X}$. In addition, the reference density of the solid ρ_0 is related to the current density ρ by $\rho = J\rho_0$, where $J = \det \mathbf{F} > 0$.

To parameterize the magnetic field, there is a choice as to which variable is considered as independent (see for instance equivalent formulations in Refs. [18,26]). In this work, the magnetic field $\mathbf{B}$ is chosen as the independent magnetic variable, which, in turn, is described in terms of the magnetic vector potential $\mathbf{A}$ by $\mathbf{B} = \text{Curl}\,\mathbf{A}$ (where the "Curl" operator is defined with respect to the undeformed configuration). This is a convenient choice

because, on one hand, $\mathbf{A}$ is work-conjugate to the current density $\mathbf{J}$ (which leads to a straightforward means of modeling the coil) and, on the other hand, it leads identically to Div $\mathbf{B}=\mathbf{0}$ (where the "Div" operator is defined with respect to the undeformed configuration). In addition, one can show by standard push-forward operations that the Eulerian magnetic field is given by $\mathbf{b}=J^{-1}\mathbf{F}\mathbf{B}$. Henceforth, unless stated otherwise, lower case variables represent Eulerian quantities, while upper case ones represent Lagrangian quantities. The conjugate stress and h-fields are defined later in this section.

Building on the works of Refs. [40,41], the total potential energy contained in V is expressed as follows:

$$\mathcal{P}(\mathbf{u},\mathbf{A})=\int_V W(\mathbf{F}(\mathbf{u}),\mathbf{B}(\mathbf{A}))\,\mathrm{d}V-\int_V(\mathbf{J}\cdot\mathbf{A}+\mathbf{f}\cdot\mathbf{u})\,\mathrm{d}V-\int_{\partial V}\mathbf{T}\cdot\mathbf{u}\,\mathrm{d}S+\frac{1}{2\mu_0\xi}\int_V(\mathrm{Div}\,\mathbf{A})^2\,\mathrm{d}V \tag{1}$$

where $\mathbf{u}$ is a kinematically admissible displacement field in the usual sense and $\mathbf{A}$ is the vector potential to be discussed in the following, while the corresponding boundary conditions are detailed in Sec. 3.3.2. This formulation is based on the eddy current approximation, which consists of neglecting the electric displacement currents in the Maxwell equations [42]. Such an approximation is valid for low-rate quasi-static loading conditions such as those in the present study. The first term captures the internal energy of the material that occupies V. The energy density W is defined for each material in the device in Sec. 3.2. The second and third terms represent external work due to body forces $\mathbf{f}$, applied traction $\mathbf{T}$, and current density $\mathbf{J}$. Inclusion of the $\mathbf{J}\cdot\mathbf{A}$ term is consistent with the source term in Ampère's law [41]. By incorporating the work done by the current density in the variational formulation, electromagnets can conveniently be modeled by assuming a continuum current density.

The last term in Eq. (1) serves to introduce the so-called Coulomb gauge constraint Div $\mathbf{A}=\mathbf{0}$. As mentioned earlier, only the rotational part (i.e., Curl) of $\mathbf{A}$ affects the magnetic field $\mathbf{B}$, and as a result, its divergence remains undetermined. To resolve this indeterminacy, several approaches have been proposed in the literature of electromagnetics using the so-called edge elements (see for instance Ref. [43] and numerous works resulting from that study). Nonetheless, such a formulation expresses the vector potential as an unknown at the edges of the element and not the nodes. In turn, the continuity of the displacement field in a finite-strain mechanical problem with multiple (perfect) interfaces requires the displacement to be defined at the nodes. This observation makes the combination of these two formulations extremely cumbersome technically. Consequently, Coulomb [44] and several other authors thereafter [44–48] have proposed the use of the last term in Eq. (1) to guarantee the uniqueness of the vector potential as well as its "continuity" across material interfaces (such as material/air/coil), without affecting in essence the primary magnetic field $\mathbf{B}$. The advantage of such a formulation allows the present form of a standard displacement-based finite element formulation to be maintained and leads to a straightforward implementation. Note further that the constraint Div $\mathbf{A}=\mathbf{0}$ may be implemented with different methods. For simplicity, in the present work, the Coulomb gauge is dealt with via the penalty method with ξ denoting the penalty parameter that should take small values for the constraint to be satisfied up to a numerical tolerance. The permeability of vacuum μ_0 is introduced simply for dimensional reasons. This term does not have physical meaning other than to enforce uniqueness of $\mathbf{A}$. In practice, the exact value of the penalty ξ does not affect numerical solutions so long as it is sufficiently small, and the corresponding term is *under-integrated* since it behaves as a strong constraint. In this study, a value $\xi=10^{-6}$ delivers converged and stable numerical results.

Then, minimization of $\mathcal{P}$ with respect to $\mathbf{u}$ and $\mathbf{A}$ implies setting the first variation of $\mathcal{P}$ equal to zero, i.e.,

$$\delta\mathcal{P}=\int_V\left(\frac{\partial W(\mathbf{F},\mathbf{B})}{\partial\mathbf{F}}\cdot\delta\mathbf{F}+\frac{\partial W(\mathbf{F},\mathbf{B})}{\partial\mathbf{B}}\cdot\delta\mathbf{B}\right)\mathrm{d}V-\int_V(\mathbf{J}\cdot\delta\mathbf{A}+\mathbf{f}\cdot\delta\mathbf{u})dV-\int_{\partial V}(\mathbf{T}\cdot\delta\mathbf{u})\mathrm{d}S+\frac{1}{\mu_0\xi}\int_V\mathrm{Div}\,\mathbf{A}\cdot\mathrm{Div}\,\delta\mathbf{A}\,\mathrm{d}V=0 \tag{2}$$

where $\delta\mathbf{F}=\mathrm{Grad}\,\delta\mathbf{u}$ and $\delta\mathbf{B}=\mathrm{Curl}\,\delta\mathbf{A}$. From this expression, the first Piola–Kirchhoff stress and Lagrangian h-field are readily identified as follows:

$$\mathbf{S}=\frac{\partial W(\mathbf{F},\mathbf{B})}{\partial\mathbf{F}},\quad\mathbf{H}=\frac{\partial W(\mathbf{F},\mathbf{B})}{\partial\mathbf{B}} \tag{3}$$

The Eulerian counterparts of these fields are obtained by standard push-forward operations [49], such that $\boldsymbol{\sigma}=J^{-1}\mathbf{S}\mathbf{F}^T$ and $\mathbf{h}=\mathbf{H}\mathbf{F}^{-T}$. Expression (2) constitutes the weak form of the mechanical equilibrium equations and Maxwell equations of magnetostatics (see detailed discussion in Ref. [50] for instance). Subsequently, the second variation of the total potential energy reads

$$\Delta\delta\mathcal{P}=\int_V\left(\Delta\mathbf{F}\cdot\frac{\partial^2W}{\partial\mathbf{F}\partial\mathbf{F}}\cdot\delta\mathbf{F}+\Delta\mathbf{F}\cdot\frac{\partial^2W}{\partial\mathbf{F}\partial\mathbf{B}}\cdot\delta\mathbf{B}+\Delta\mathbf{B}\cdot\frac{\partial^2W}{\partial\mathbf{B}\partial\mathbf{F}}\cdot\delta\mathbf{F}+\Delta\mathbf{B}\cdot\frac{\partial^2W}{\partial\mathbf{B}\partial\mathbf{B}}\cdot\delta\mathbf{B}\right)\mathrm{d}V+\frac{1}{\mu_0\xi}\int_V\mathrm{Div}\,\Delta\mathbf{A}\cdot\mathrm{Div}\,\delta\mathbf{A}\,\mathrm{d}V \tag{4}$$

Use of expressions (2) and (4) allows for a standard finite element discretization and resolution by standard Newton–Raphson schemes (see for instance details in Ref. [46]). In the present example, a three-dimensional finite-strain magneto-elastic user element is implemented in ABAQUS.

3.2 Constitutive Models. Each component of the BVP at hand is modeled by use of a suitable constitutive model defined for each material. Following recent work [24,26], the energy density per unit referential volume of a magneto-elastic material can be partitioned into contributions from mechanical, magnetic, and vacuum terms, i.e.,

$$W(\mathbf{F},\mathbf{B})=\Psi^{\mathrm{mech}}(I_1,J)+\Psi^{\mathrm{mag}}(J,I_5)+\Psi^{\mathrm{vac}}(J,I_5) \tag{5}$$

The corresponding magneto-mechanical invariants are defined as follows:

$$I_1=\mathbf{F}:\mathbf{F},\quad J=\det\mathbf{F},\quad I_5=\mathbf{F}\mathbf{B}\cdot\mathbf{F}\mathbf{B} \tag{6}$$

For simplicity in the numerical implementation, a quasi-incompressible form of the models is used. That is also in accord with experiments [33] that show a quasi-incompressible response of the present MREs (i.e., $J\approx1$ but not equal to unity).

Each of the four materials in the device (MRE, iron, air, and coil) is modeled *with the same energy density* defined in Eq. (5), but with different material coefficients. Since the core and coil are modeled as rigid, and the air is modeled with negligible stiffness, the mechanical contribution Ψ^{mech} is most relevant for the MRE. Consequently, the mechanical energy density is chosen to model the MRE and is taken from the family of models proposed in Ref. [51]. The polymeric matrix phase is modeled as a Neo–Hookean material and the iron particles as mechanically rigid. The corresponding continuum (homogenized) energy density for

Table 1 Material properties

Property	MRE	Iron	Coil	Air
G_m (MPa)	0.0075	0.75	0.75	3.75×10^{-5}
G'_m (MPa)	1.5	3	3	7.5×10^{-5}
$\mu_0\, m_s$ (T)	–	2.5	0	0
χ	0.235	2000	0	0
c	0.08	–	–	–
$\mu_0\, m^s_p$ (T)	2.5	–	–	–
χ_p	30	–	–	–

the MRE reads

$$\Psi^{\text{mech}}(I_1, J) = \frac{G_m}{2(1-c)^{5/2}}[I_1 - 3 - 2\ln J] + \frac{G'_m}{2(1-c)^6}(J-1)^2 \tag{7}$$

where G_m and G'_m are the Lamé moduli of the polymer matrix phase and c denotes the volume fraction of the particles. Note that the magneto-elastic response depends on the particle content expressed as a volume fraction c and not as phr. Nevertheless, one can obtain the first from the second by using the density of the matrix $\rho_m = 1070\,\text{kg/m}^3$ and the particles $\rho_p = 7874\,\text{kg/m}^3$ [33]. Table 1 summarizes the moduli used to model each material. To model the quasi-incompressible matrix of the MRE, the bulk modulus is taken as $G'_m = 200G_m$. The shear modulus of the matrix is fit as $G_m = 0.0075$ MPa based on the experiment without the iron core, which is discussed in Sec. 4.1. The coil and core are modeled as nearly rigid by taking sufficiently large values for the moduli in Eq. (7).

Ideally, the air should have zero stiffness. In this modeling framework, however, a very soft material description for the air is employed, following the existing literature [20]. That requires small, but nonetheless finite values for the mechanical air properties. As a consequence, the stiffness of the air affects the solution as a whole, but only weakly. This effect only leads to the use of slightly larger material properties (e.g., magnetic susceptibility and shear modulus) for the MRE layer for a good calibration of the model. Such a deviation from the actual properties is on the order of a couple of percents. Alternative ways to deal with the air [24] may improve on this aspect; however, the difficulty in the present problem lies in the very complex air geometry that results from the device itself. Thus, the simple but fairly efficient approach of a very soft mechanical energy has been used for the air.

In turn, the purely magnetic contribution is taken as follows:

$$\Psi^{\text{mag}}(J, I_5) = -\frac{\chi}{2\mu_0(1+\chi)}\frac{I_5}{J^2}\,{}_2\mathcal{F}_1\left[\frac{1}{k}, \frac{2}{k}, 1+\frac{2}{k}, -\left(\frac{\chi}{\mu_0(1+\chi)m^s}\frac{\sqrt{I_5}}{J}\right)^k\right] \tag{8}$$

where m^s and χ are the magnetic saturation and magnetic susceptibility of the MRE, respectively, while ${}_2\mathcal{F}_1$ is the hypergeometric function. The hypergeometric function can be used to recover a wide range of magnetic responses from Langevin to hyperbolic tangent. For the MRE, a value $k = 6$ defines accurately the magnetization curve, as discussed in Ref. [26]. The saturation and susceptibility of the MRE can be derived from the matrix and particle constituents as follows [26]:

$$m^s = cm^s_p, \quad \chi = \frac{3c\chi_p}{(2+c)+(1-c)(1+\chi_p)} \tag{9}$$

where the particles have volume fraction c, saturation magnetization m^s_p, and magnetic susceptibility χ_p. The hypergeometric function is also suitable to model the magnetic response of iron, for which $k = 2$ is used. Finally, the coil and air are not magnetic. Table 1 summarizes the magnetic parameters used for each material. Specifically, a very large susceptibility is used for the iron taken from standard handbooks.

Finally, the contribution of the magnetic field in vacuum is expressed as follows:

$$\Psi^{\text{vac}}(J, I_5) = \frac{I_5}{2\mu_0 J} \tag{10}$$

This term is present in all materials and serves to describe the presence of the background magnetic field [40].

It is remarked here that a more elaborate constitutive law could also include a coupling term Ψ^{couple} in Eq. (5) to describe magnetostrictive coupling in the MRE. For this specific BVP, however, the coupling term has been shown (not included here for brevity) to have negligible contribution to the simulations (see also Ref. [24]) due to the fairly small strains (but significant rotations and thus the finite-strain framework) in the MRE disk. Thus, the coupled term in the constitutive equation is omitted, and the reader is referred to Ref. [26] for a more detailed discussion of this point.

3.3 Numerical Implementation. A finite element model is implemented in ABAQUS via a user-element routine to represent the device. The model describes as faithfully as possible the three-dimensional BVP of the device, with the sole input being the current applied to the electromagnetic coil. To capture this problem setting, the volume containing the MRE layer, coil, iron core and casing, and surrounding air must be modeled. The various aspects of the implementation are discussed in this section.

3.3.1 Meshing. A user element, based on the variational principle of Sec. 3.1 and constitutive model of Sec. 3.2, is used to model all materials in the problem. The user element is implemented as an eight-node hexahedral element with a 2×2 Gauss integration rule (except for the Coulomb gauge term that uses a single Gauss point in the middle of the element). There are six degrees-of-freedom per node describing the displacements u_i ($i = 1, 2, 3$) and magnetic vector potential A_i ($i = 1, 2, 3$). For elements belonging to the MRE phase, which is quasi-incompressible, reduced integration is also used for the term $(J-1)^2$.

By employing quarter-symmetry, a quarter-cylindrical domain is used to encompass the device and surrounding air. For resolving accurately the magnetic field, convergence is considered with respect to the domain size and use of Neumann and Dirichlet type boundary conditions for the vector potential (not shown here for brevity). A domain with a radius of 112 mm and a height of 161 mm is found to be sufficiently large, thereby leading to no differences in the MRE response irrespective of the type of far boundary conditions on the vector potential. As a consequence, further extending the domain has negligible effects on the solution. Figure 6 shows the mesh, with each material highlighted. The device configuration with the core present is depicted in this figure. For the configuration with the core inserted, a mesh with 181,576 elements and 192,105 nodes is used. For the device configuration without the core, a mesh with 160,646 elements and 171,000 nodes is used. In both cases, the total size of the problem is on the order of 10^6 degrees-of-freedom (as there are 6 degrees-of-freedom per node).

The mesh represents all components of the experimental setup shown in Fig. 1(*b*), except the plastic casing. Since the plastic casing is nonmagnetic, it exhibits negligible deformation and does not interfere with the important parts of the device (e.g., MRE, core, coil). For this reason, it is replaced with undeformable air in the numerical model. To model the clamping of the MRE by the plastic casing, displacement boundary conditions are applied along the outer edge of the MRE surface, as indicated by the

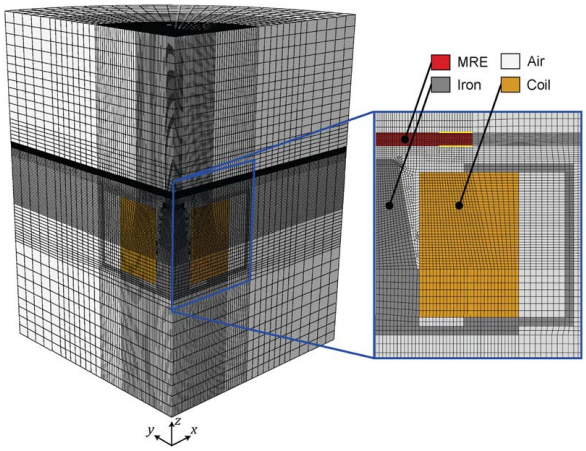

Fig. 6 Finite element mesh for the device configuration with the core present

lighter-colored (yellow) segments appearing at the top and bottom of the edge of the MRE layer in Fig. 6.

3.3.2 Boundary Conditions. Three sets of boundary conditions are applied to the domain. The first set enforces symmetry along the xz and yz planes. The displacement degrees-of-freedom of nodes on these faces are constrained, such that no displacement can occur normal to the plane of symmetry. To enforce symmetry of the magnetic field, the corresponding boundary conditions on the vector potential read

$$A_1(y=0)=0, \quad \left.\frac{\partial A_2}{\partial y}\right|_{y=0}=0, \quad A_1(y=0)=0 \tag{11}$$

$$\left.\frac{\partial A_1}{\partial x}\right|_{x=0}=0, \quad A_2(x=0)=0, \quad A_3(x=0)=0 \tag{12}$$

These conditions are consistent with tangential continuity [47,48] of $\mathbf{A}$ across the symmetry planes (i.e., $\mathbf{A}\times\mathbf{n}=\mathbf{0}$ with $\mathbf{n}$ denoting the normal to the symmetry plane).

The second set of boundary conditions is applied to the far-field boundary, which includes the top, bottom, and outer radial surface of the quarter-cylindrical domain. On the far-field boundary, either homogeneous Neumann or Dirichlet conditions can be enforced on all vector potential components. In this study, a sufficiently large domain is employed. Thus, the obtained solutions are independent of the far boundary conditions on the vector potential.

The third set of boundary conditions models the clamping of the MRE by the plastic casing. Along the lower yellow segment on the MRE in Fig. 6, the z-displacement is fixed. Along the upper yellow segment, a vertical displacement of -1 mm is applied following the experimental setup. Sliding is prevented by fixing all displacement components on the inner radius of the lower yellow segment. In reality, the clamping of the MRE by the casing may exhibit a more complex behavior. As the device is loaded and the MRE is pulled downward by the magnetic field, the grip of the casing may not be perfect and the MRE may slide with respect to the casing. A more complex model taking into account approximately the friction (see for instance, Ref. [24]) could perhaps capture more accurately the clamping boundary condition. Nonetheless, the focus of this study is to capture the overall behavior of the device BVP, and this simplified boundary condition will prove sufficient.

3.3.3 Loading. The source of loading in the device is the current applied to the electromagnetic coil. There is a trade-off regarding the level of detail of the model: more details can always be added to the model to better capture the experimental setting at the cost of working with an overly complex model. Instead of modeling individual loops of wire in the coil, a continuum model is adopted. The continuum model assumes axisymmetry and uniform current density, which provides a reasonable approximation for a thick coil with many turns [52]. Current density in the coil is approximated by

$$\mathbf{J}=\mathrm{J}_\Theta\mathbf{e}_\Theta, \quad \mathrm{J}_\Theta=\frac{NI}{h(r_o-r_i)} \tag{13}$$

In this expression, J_Θ is the current density along the angular direction $\mathbf{e}_\Theta$ of a cylindrical coordinate system describing the coil. The current in each of the N turns of the wire is I and $r_i=10$ mm, $r_o=32.5$ mm, and $h=33$ mm are the inside radius, outside radius, and height of the coil, respectively.

To better capture the experimental setting, self-weight of the MRE is also considered, which is implemented as a body force $\mathbf{f}=-\rho g\mathbf{e}_3$ in the z direction, where $\rho=(1-c)\rho_\mathrm{m}+c\rho_\mathrm{p}$ and g is acceleration due to gravity. Loading of the BVP is performed as a three-step process. First, the clamp boundary condition is applied, representing the mounting of the MRE in the plastic casing. The second step is to apply gravitational loading. Finally, the current I is applied to the coil, producing a magnetic field that loads the MRE.

4 Discussion

4.1 Comparison Between Experimental and Numerical Results. Figure 7 compares experimental and numerical vertical displacements at the center of the top surface of the isotropic MRE layer, with and without the core present. The constitutive model requires the calibration of the shear modulus of the MRE matrix G_m only, while the rest is taken from handbooks and earlier studies as reported in Table 1. To identify the value of G_m, the experimental data from the "coil-only" configuration is used to obtain a fit. A shear modulus of $G_\mathrm{m}=7.5$ kPa provides good agreement between the experiment and simulation for the "coil-only" configuration. This value is in close agreement with earlier work using similar MRE materials [24,33].

The model additionally demonstrates predictive capability, which is evident through the good agreement between the experiment and simulations for the "coil plus core" configuration. This agreement is rather impressive given that the magnetic fields in the configurations with and without the core are very different, as discussed in Sec. 4.2. It is noted that no further calibration is performed to obtain the response with the core.

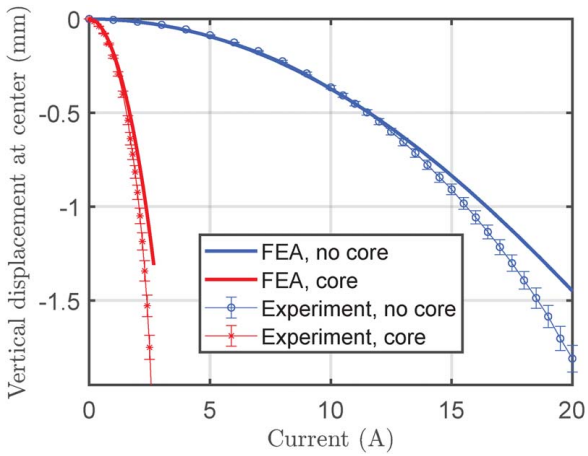

Fig. 7 Comparison between experiments and finite element simulations for device configurations with and without the core: vertical displacement at the center of the upper surface of the isotropic MRE layer

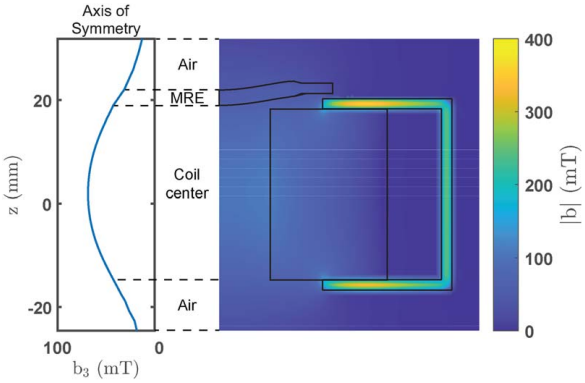

Fig. 8 Eulerian magnetic field *b* plotted on the *xz* face and along the axis of symmetry. The field corresponds to an applied current *I* = 20 A in the "coil-only" configuration.

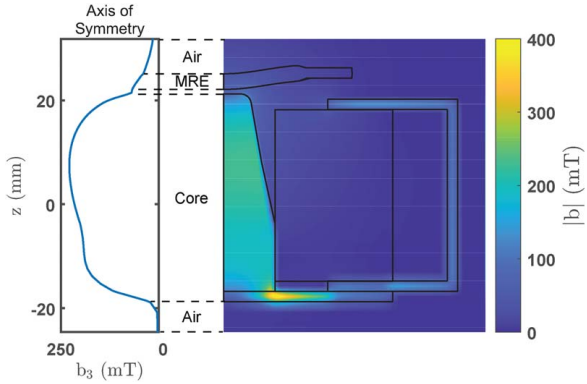

Fig. 10 Eulerian magnetic field *b* plotted on the *xz* face and along the axis of symmetry. The field corresponds to an applied current *I* = 2.7 A in the "coil plus core" configuration.

Specifically, the simulations are in excellent agreement with the experiments for a large range of applied current. As the MRE displacement increases, there is some divergence between the experimental and numerical curves (see Fig. 7). This is due to the complex boundary conditions of the plastic casing gripping the MRE. In the experiment, the MRE is not perfectly gripped by the casing, and some sliding is inevitable. This sliding is not modeled in the present simulation, thus leading to a slightly stiffer response as the MRE disk displaces.

4.2 Magnetic Fields. The simulations are now used to provide further insight into aspects of the device that are out of reach experimentally, such as a detailed description of the induced magnetic fields. Figures 8 and 9 show the Eulerian magnetic fields **b** and **h** on the *xz* face of the mesh (refer to Fig. 6) in the "coil-only" configuration corresponding to a 20 A applied current. Similarly, Figs. 10 and 11 show the Eulerian magnetic fields on the *xz* face in the "coil plus core" configuration corresponding to a 2.7 A applied current.

The simulated magnetic fields highlight the role of the core. By focusing but also intensifying the magnetic field near the MRE, the core leads to stronger attractive magnetic forces toward the MRE disk and thus to larger deflections at much lower applied currents. In contrast, the magnetic fields created by the coil in the "coil-only" configuration strongly diminish near the MRE layer. In addition, the fields are able to show the effect of surrounding materials, such as the iron casing (see, for instance, Figs. 8 and 9) as well as the effect of the iron core geometry, which exhibits a rather nonuniform internal distribution of the magnetic field *b* (see Fig. 10).

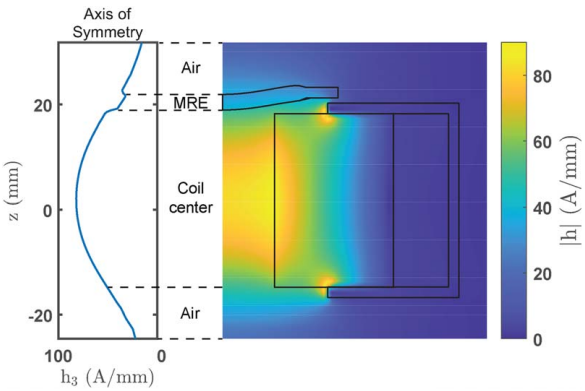

Fig. 9 Eulerian *h*-field plotted on the *xz* face and along the axis of symmetry. The field corresponds to an applied current *I* = 20 A in the "coil-only" configuration.

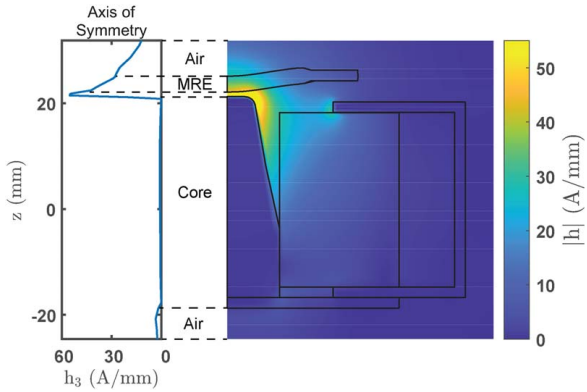

Fig. 11 Eulerian *h*-field plotted on the *xz* face and along the axis of symmetry. The field corresponds to an applied current *I* = 2.7 A in the "coil plus core" configuration.

From a numerical standpoint, Figs. 8–11 demonstrate that highly nonuniform magnetic fields can be modeled by the presented formulation. Furthermore, jumps in the magnetic field at interfaces are properly captured with the proposed formulation. This is evident in the *h*-fields, where there are jumps on the top and bottom of the MRE layer as expected by the tangential-only continuity required for those fields.

5 Conclusion

In this study, experiments and numerical simulations of a model device composed of an electromagnetic coil that deflects a magnetorheological elastomer layer are presented. Experimental results show that particle field structuring and their associated instabilities do not present any advantage in the proposed configuration. The fact that an isotropic MRE performs best is counterintuitive considering the results from material characterization (see Ref. [33]), but it is useful from a fabrication standpoint. Furthermore, the experiments show that the presence of an iron core inside the coil concentrates the magnetic field near the layer to cause large deflections at smaller applied currents.

Alongside the experiments, a general framework for numerical simulations of magneto-mechanical BVPs involving coils is presented. A magnetic vector potential variational framework is proposed, from which a three-dimensional magneto-elastic finite element model is derived at finite strains and arbitrary magnetic fields. The numerical implementation introduces two key features that contribute to its versatility. First, the external work due to the

current density is included in a Lagrangian formulation, allowing electromagnets to be modeled using an eddy current approximation. Second, a Coulomb gauge is enforced using a penalty term, ensuring uniqueness of the vector potential. Together, these terms allow for highly nonuniform magnetic fields generated by electromagnets to be captured along with a finite-strain Lagrangian formulation.

The numerical implementation allows for versatile modeling of nontrivial magneto-mechanical BVPs since everything, from electromagnets to MREs to magnetic metals, can be modeled with a single user-element definition. Thus, simulations of the MRE device could be performed in a setting that parallels the experiment, where the only controlled variable is the current that is applied to the electromagnet. The model shows very good agreement with experiments in both of the considered device configurations, i.e., with and without the iron core. Here, it is important to recall that constitutive calibration is only performed in the "coil-only" configuration, thereby circumventing the need for a separate material characterization procedure. In view of this, the model shows powerful predictive capability through agreement with experiment in the "coil plus core" configuration. Furthermore, the simulations provide insights that cannot be obtained experimentally, such as detailed magnetic fields, which properly reproduce jumps at material interfaces. Overall, the proposed simulation framework proves to be an accurate and robust tool for modeling complex BVPs involving MREs and, thus, constitutes a step toward designing more efficient MRE-based devices.

Acknowledgment

The authors acknowledge Tobias Pössinger for designing the coil used in the study and constructive discussions with Professor N. Triantafyllidis. K.D. acknowledges the support from the European Research Council (ERC) under the European Union's Horizon 2020 research and innovation program (Grant No. 636903 – MAGNETO). The computational part of this work was supported by the ANR, France, under contract number ANR-10-EQPX-37 and the code developed for the numerical simulations in this work is available in Ref. [53]. The work of C.D. was initially supported by the Ecole Polytechnique and its Foundation during AY 2017–2018 through the dual MS program with Caltech and subsequently by the Solid Mechanics Laboratory (LMS) of the Ecole.

Conflicts of Interest

There are no conflicts of interest.

Data Availability Statement

The datasets generated and supporting the findings of this article are obtainable from the corresponding author upon reasonable request. The data and information that support the findings of this article are freely available at: https://www.doi.org/10.5281/zenodo.4597372. The authors attest that all data for this study are included in the paper. Data provided by a third party listed in Acknowledgment.

References

[1] Rigbi, Z., and Jilken, L., 1983, "The Response of an Elastomer Filled With Soft Ferrite to Mechanical and Magnetic Influences," J. Magn. Magn. Mater., **37**(3), pp. 267–276.
[2] Li, Y., Li, J., Li, W., and Du, H., 2014, "A State-of-the-Art Review on Magnetorheological Elastomer Devices," Smart Mater. Struct., **23**(12), p. 123001.
[3] Elie, L. D., Ginder, J. M., Nichols, M. E., and Stewart, W. M., 2002, "Variable Stiffness Bushing Using Magnetorheological Elastomers," European Patent No. EP0784163A.
[4] Crist, R. J., 2009, "Active Vibrational Damper," U.S. Patent No. 75,846,85B.
[5] Marur, P. R., 2013, "Magneto-Rheological Elastomer-Based Vehicle Suspension," U.S. Patent No. 20,130,087.
[6] Thorsteinsson, F., Gudmundsson, I., and Lecomte, C., 2015, "Prosthetic and Orthotic Devices Having Magnetorheological Elastomer Spring With Controllable Stiffness," U.S. Patent No. 90,787,34B.
[7] Ginder, J. M., Nichols, M. E., Elie, L. D., and Clark, S. M., 2000, "Controllable-Stiffness Components Based on Magnetorheological Elastomers," SPIE's 7th Annual International Symposium on Smart Structures and Materials, Newport Beach, CA, June 22, International Society for Optics and Photonics, pp. 418–425.
[8] Farshad, M., and Le Roux, M., 2004, "A New Active Noise Abatement Barrier System," Polym. Test., **23**(7), pp. 855–860.
[9] Böse, H., Rabindranath, R., and Ehrlich, J., 2012, "Soft Magnetorheological Elastomers as New Actuators for Valves," J. Intell. Mater. Syst. Struct., **23**(9), pp. 989–994.
[10] Stepanov, G., Kramarenko, E. Y., and Semerenko, D., 2013, "Magnetodeformational Effect of the Magnetoactive Elastomer and Its Possible Applications," J. Phys. Conf. Series, **412**, p. 012031.
[11] Ahamed, R., Choi, S.-B., and Ferdaus, M. M., 2018, "A State of Art on Magneto-Rheological Materials and Their Potential Applications," J. Intell. Mater. Syst. Struct., **29**(10), pp. 2051–2095.
[12] Kim, Y., Parada, G. A., Liu, S., and Zhao, X., 2019, "Ferromagnetic Soft Continuum Robots," Sci. Rob., **4**(33), p. eaax7329.
[13] Ren, Z., Hu, W., Dong, X., and Sitti, M., 2019, "Multi-Functional Soft-Bodied Jellyfish-Like Swimming," Nat. Commun., **10**(1), p. 2703.
[14] Xu, T., Zhang, J., Salehizadeh, M., Onaizah, O., and Diller, E., 2019, "Millimeter-Scale Flexible Robots With Programmable Three-Dimensional Magnetization and Motions," Sci. Rob., **4**(29), p. eaav4494.
[15] Borcea, L., and Bruno, O., 2001, "On the Magneto-Elastic Properties of Elastomer–Ferromagnet Composites," J. Mech. Phys. Solids, **49**(12), pp. 2877–2919.
[16] Danas, K., Kankanala, S., and Triantafyllidis, N., 2012, "Experiments and Modeling of Iron-Particle-Filled Magnetorheological Elastomers," J. Mech. Phys. Solids, **60**(1), pp. 120–138.
[17] Kalina, K. A., Metsch, P., and Kästner, M., 2016, "Microscale Modeling and Simulation of Magnetorheological Elastomers at Finite Strains: A Study on the Influence of Mechanical Preloads," Int. J. Solids Struct., **102–103**, pp. 286–296.
[18] Danas, K., 2017, "Effective Response of Classical, Auxetic and Chiral Magnetoelastic Materials by Use of a New Variational Principle," J. Mech. Phys. Solids, **105**, pp. 25–53.
[19] Lefèvre, V., Danas, K., and Lopez-Pamies, O., 2017, "A General Result for the Magnetoelastic Response of Isotropic Suspensions of Iron and Ferrofluid Particles in Rubber, With Applications to Spherical and Cylindrical Specimens," J. Mech. Phys. Solids, **107**, pp. 343–364.
[20] Keip, M.-A., and Rambausek, M., 2017, "Computational and Analytical Investigations of Shape Effects in the Experimental Characterization of Magnetorheological Elastomers," Int. J. Solids Struct., **121**, pp. 1–20.
[21] Kalina, K. A., Brummund, J., Metsch, P., Kästner, M., Borin, D. Y., Linke, J. M., and Odenbach, S., 2017, "Modeling of Magnetic Hystereses in Soft MREs Filled With NdFeB Particles," Smart Mater. Struct., **26**(10), p. 105019.
[22] Kim, Y., Yuk, H., Zhao, R., Chester, S. A., and Zhao, X., 2018, "Printing Ferromagnetic Domains for Untethered Fast-Transforming Soft Materials," Nature, **558**(7709), pp. 274–279.
[23] Zhao, R., Kim, Y., Chester, S. A., Sharma, P., and Zhao, X., 2019, "Mechanics of Hard-Magnetic Soft Materials," J. Mech. Phys. Solids, **124**, pp. 244–263.
[24] Psarra, E., Bodelot, L., and Danas, K., 2019, "Wrinkling to Crinkling Transitions and Curvature Localization in a Magnetoelastic Film Bonded to a Non-Magnetic Substrate," J. Mech. Phys. Solids, **133**, p. 103734.
[25] Karami Mohammadi, N., Galich, P. I., Krushynska, A. O., and Rudykh, S., 2019, "Soft Magnetoactive Laminates: Large Deformations, Transverse Elastic Waves and Band Gaps Tunability by a Magnetic Field," ASME J. Appl. Mech., **86**(11), p. 111001.
[26] Mukherjee, D., Bodelot, L., and Danas, K., 2020, "Microstructurally-Guided Explicit Continuum Models for Isotropic Magnetorheological Elastomers With Iron Particles," Int. J. Non-Linear Mech., **120**, p. 103380.
[27] Lefèvre, V., Danas, K., and Lopez-Pamies, O., 2020, "Two Families of Explicit Models Constructed From a Homogenization Solution for the Magnetoelastic Response of MREs Containing Iron and Ferrofluid Particles," Int. J. Non-Linear Mech., **119**, p. 103362.
[28] Rambausek, M., and Danas, K., 2021, "Bifurcation of Magnetorheological Film–Substrate Elastomers Subjected to Biaxial Pre-Compression and Transverse Magnetic Fields," Int. J. Non-Linear Mech., **128**, p. 103608.
[29] Chen, W., and Wang, L., 2020, "Theoretical Modeling and Exact Solution for Extreme Bending Deformation of Hard-Magnetic Soft Beams," ASME J. Appl. Mech., **87**(4), p. 041002.
[30] Zhang, R., Wu, S., Ze, Q., and Zhao, R., 2020, "Micromechanics Study on Actuation Efficiency of Hard-Magnetic Soft Active Materials," ASME J. Appl. Mech., **87**(9), p. 091008.
[31] Schubert, G., and Harrison, P., 2015, "Large-Strain Behaviour of Magneto-Rheological Elastomers Tested Under Uniaxial Compression and Tension, and Pure Shear Deformations," Polym. Test., **42**, pp. 122–134.
[32] Psarra, E., Bodelot, L., and Danas, K., 2017, "Two-Field Surface Pattern Control Via Marginally Stable Magnetorheological Elastomers," Soft Matter, **13**(37), pp. 6576–6584.
[33] Bodelot, L., Voropaieff, J.-P., and Pössinger, T., 2018, "Experimental Investigation of the Coupled Magneto-Mechanical Response in Magnetorheological Elastomers," Exp. Mech., **58**(2), pp. 207–221.

[34] Bastola, A. K., and Hossain, M., 2020, "A Review on Magneto-Mechanical Characterizations of Magnetorheological Elastomers," Compos. Part B: Eng., **200**, p. 108348.
[35] Pössinger, T., Bolzmacher, C., Bodelot, L., and Triantafyllidis, N., 2014, "Influence of Interfacial Adhesion on the Mechanical Response of Magneto-Rheological Elastomers at High Strain," Microsyst. Technol., **20**(4), pp. 803–814.
[36] Feng, J., Xuan, S., Lv, Z., Pei, L., Zhang, Q., and Gong, X., 2018, "Magnetic-Field-Induced Deformation Analysis of Magnetoactive Elastomer Film by Means of DIC, LDV, and FEM," Ind. Eng. Chem. Res., **57**(9), pp. 3246–3254.
[37] Sutton, M. A., Orteu, J.-J., and Schreier, H. W., 2009, *Image Correlation for Shape, Motion and Deformation Measurements. Basic Concepts, Theory and Applications*, Springer, New York.
[38] Varga, Z., Filipcsei, G., and Zrínyi, M., 2006, "Magnetic Field Sensitive Functional Elastomers With Tuneable Elastic Modulus," Polymer, **47**(1), pp. 227–233.
[39] Danas, K., and Triantafyllidis, N., 2014, "Instability of a Magnetoelastic Layer Resting on a Non-Magnetic Substrate," J. Mech. Phys. Solids, **69**, pp. 67–83.
[40] Dorfmann, A., and Ogden, R., 2003, "Magnetoelastic Modelling of Elastomers," Eur. J. Mech. A/Solids, **22**(4), pp. 497–507.
[41] Thomas, J. D., and Triantafyllidis, N., 2009, "On Electromagnetic Forming Processes in Finitely Strained Solids: Theory and Examples," J. Mech. Phys. Solids, **57**(8), pp. 1391–1416.
[42] Ammari, H., Buffa, A., and Nédélec, J.-C., 2000, "A Justification of Eddy Currents Model for the Maxwell Equations," SIAM J. Appl. Math., **60**(5), pp. 1805–1823.
[43] Nédélec, J.-C., 1980, "Mixed Finite Elements in $\mathbb{R}^3$," Numer. Math., **35**, pp. 315–341.
[44] Coulomb, J.-L., 1981, "Finite Elements Three Dimensional Magnetic Field Computation," IEEE Trans. Magn., **17**(6), pp. 3241–3246.
[45] Biro, O., and Preis, K., 1989, "On the Use of the Magnetic Vector Potential in the Finite-Element Analysis of Three-Dimensional Eddy Currents," IEEE Trans. Magn., **25**(4), pp. 3145–3159.
[46] Landis, C. M., 2002, "A New Finite-Element Formulation for Electromechanical Boundary Value Problems," Int. J. Numer. Methods Eng., **55**(5), pp. 613–628.
[47] Semenov, A. S., Kessler, H., Liskowsky, A., and Balke, H., 2006, "On a Vector Potential Formulation for 3D Electromechanical Finite Element Analysis," Commun. Numer. Methods Eng., **22**(5), pp. 357–375.
[48] Stark, S., Semenov, A. S., and Balke, H., 2015, "On the Boundary Conditions for the Vector Potential Formulation in Electrostatics," Int. J. Numer. Methods Eng., **102**(11), pp. 1704–1732.
[49] Kankanala, S., and Triantafyllidis, N., 2004, "On Finitely Strained Magnetorheological Elastomers," J. Mech. Phys. Solids, **52**(12), pp. 2869–2908.
[50] Bustamante, R., Dorfmann, A., and Ogden, R. W., 2008, "On Variational Formulations in Nonlinear Magnetoelastostatics," Math. Mech. Solids, **13**, pp. 725–745.
[51] Lopez-Pamies, O., Goudarzi, T., and Danas, K., 2013, "The Nonlinear Elastic Response of Suspensions of Rigid Inclusions in Rubber: II—A Simple Explicit Approximation for Finite-Concentration Suspensions," J. Mech. Phys. Solids, **61**(1), pp. 19–37.
[52] Forbes, L. K., Crozier, S., and Doddrell, D. M., 1997, "Rapid Computation of Static Fields Produced by Thick Circular Solenoids," IEEE Trans. Magn., **33**(5), pp. 4405–4410.
[53] Dorn, C., Bodelot, L., and Danas, K., 2021, "Abaqus UEL Subroutine for a Soft MRE Device Comprising a Coil and Iron Core Using the Vector Potential in Three-Dimensions."